Heat convection in a vertical channel: Plumes versus turbulent diffusion

M. Gibert,[a)] H. Pabiou,[b)] J.-C. Tisserand, B. Gertjerenken,[c)] B. Castaing, and F. Chillà[d)]
Université de Lyon, ENS Lyon, CNRS 46 Allée d'Italie, 69364 Lyon Cedex 7, France

Following a previous study [Gibert *et al.*, Phys. Rev. Lett. **96**, 084501 (2006)], convective heat transfer in a vertical channel of moderate dimensions follows purely inertial laws. It would be therefore a good model for convective flows of stars and ocean. Here we report new measurements on this system. We use an intrinsic length in the definition of the characteristic Rayleigh and Reynolds numbers. We explicit the relation between this intrinsic length and the thermal correlation length. Using particle imaging velocimetry, we show that the flow undergoes irregular reversals. We measure the average velocity profiles and the Reynolds stress tensor components. The momentum flux toward the vertical walls seems negligible compared to the shear turbulent stress. A mixing length theory seems adequate to describe the horizontal turbulent heat and momentum fluxes, but fails for the vertical ones. We propose a naive model for vertical heat transport inspired by the Knudsen regime in gases. © *2009 American Institute of Physics*. [DOI: 10.1063/1.3085812]

I. INTRODUCTION

The Rayleigh–Bénard flow, heat convection between two horizontal plates at different temperatures T_h and T_c ($T_h - T_c = \Delta T$), has long been the only paradigm for laboratory studies of thermal convection.[1–3] Recent controversies[2,4–6] concerning the occurrence of the so-called Kraichnan regime[7] stressed the importance of having a better knowledge of the bulk flow, far from the plates.[8,9] However, global quantities such as the Nusselt number (Nu)

$$\mathrm{Nu} = \frac{QH}{\lambda \Delta T} \tag{1}$$

are mainly controlled by the neighborhood of the plates, where the viscosity weakens the convection. The Nusselt number compares the heat flux Q to the purely diffusive one $\lambda \Delta T / H$, where λ is the fluid thermal conductivity, and H the vertical distance between plates.

On the other hand, natural convection, such as occurring in stars or planet's atmospheres, is often free of plates. Evaluating heat fluxes generated in such conditions is of prime importance for elucidating the behavior of these systems. In this respect, heat (or mass) convection in a vertical channel[10–12] is closer to these flows. Even if the width d of the channel introduces a characteristic length, the heat flux is everywhere convective, if one excludes the poorly pertinent vertical boundary layers, in contradistinction with the neighborhood of Rayleigh–Bénard plates. Note that a vertical access pit of an underground quarry[13] is another seminatural example of such a system.

The characteristic nondimensional numbers have here a slightly different definition. Out of end effects, a constant vertical temperature gradient $\beta = -\partial T / \partial z$ is expected to drive the heat flux, which gives the Nusselt number

$$\mathrm{Nu} = \frac{Q}{\lambda \beta}. \tag{2}$$

One of the control parameters is the Prandtl number $\mathrm{Pr} = \nu / \kappa$, where ν is the kinematic viscosity and κ the heat diffusivity. The second control parameter is the Rayleigh number

$$\mathrm{Ra} = \frac{g \alpha \beta L^4}{\nu \kappa}, \tag{3}$$

where g is the gravitational acceleration and α the constant pressure thermal expansion coefficient. The choice of the characteristic length L has to be done. It could be taken as d, the width of the channel, which *a priori* appears as the only available length. However, our previous study[12] shows that results are clearer when a different choice is made,

$$L = aL_o \quad \text{with} \quad L_o = \frac{\theta}{\beta}, \tag{4}$$

where θ is a root mean squared temperature fluctuation which will be precised later. In the same study, a characteristic time τ_o was evidenced in the spectrum of temperature fluctuations. Two hypotheses were made for interpreting the data. First, for considering θ as a temperature, we had to assume that the correlation length is relatively short. Second, we assumed that we could choose the factor a in such a way that L / τ_o be the rms velocity V_{rms}. We thus assumed

$$V_{\mathrm{rms}} = \frac{a\theta}{\beta \tau_o}. \tag{5}$$

We grossly estimated it from one single particle imaging velocimetry (PIV) experiment. We shall see that the present experiments yield a different value for a, but confirm that it can be considered as constant. With L / τ_o representing the rms velocity, we can define a Reynolds number,

$$\mathrm{Re} = \frac{L^2}{\nu \tau_o}. \tag{6}$$

a)Also at MPI-DS (LFPN) Göttingen.
b)Also at Université de Lyon, CNRS.
c)Also at Carl von Ossietzky Universität, Oldenburg.
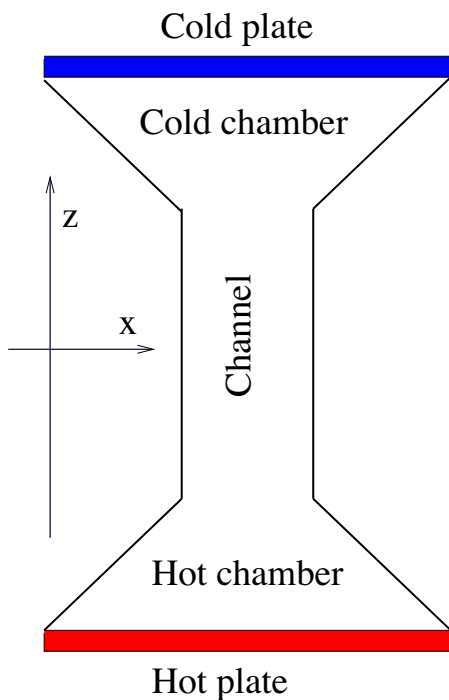d)Electronic mail: francesca.chilla@ens-lyon.fr.

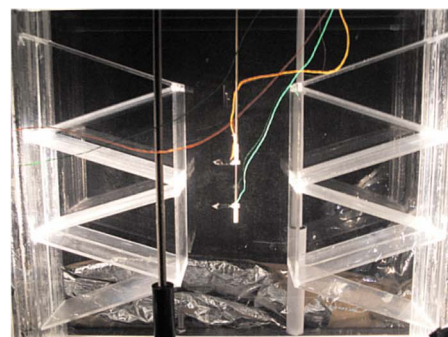FIG. 1. (Color online) Schematic of both cells, clarifying the notations.

FIG. 2. (Color online) (a) Picture of the first cell (without the insulation and the thermal screen). The L structures used for temperature correlation measurements are shown in the channel. (b) Picture of the second cell (without the insulation). The short version of the bridge (5 cm high ×2.5 cm wide) can be seen in the channel.

The important point is that this Re is obtained only through thermal measurements, within the same experiments giving Nu.

The present paper has several purposes. After a detailed presentation of the various experimental techniques and set-ups, we examine the above hypothesis, through a direct measurement of the correlation length. Then we compare the previously[12] measured Nu and Re with those obtained with a smaller cell, having a different aspect ratio. A statistical study of the velocity field follows, which allows us to determine a characteristic velocity profile, and the Reynolds stresses. From these Reynolds stresses and their horizontal (x) dependences, a horizontal temperature profile can be determined, as well as the corresponding horizontal heat flux. Before the conclusion, we examine these results from the point of view of the Prandtl mixing length theory.
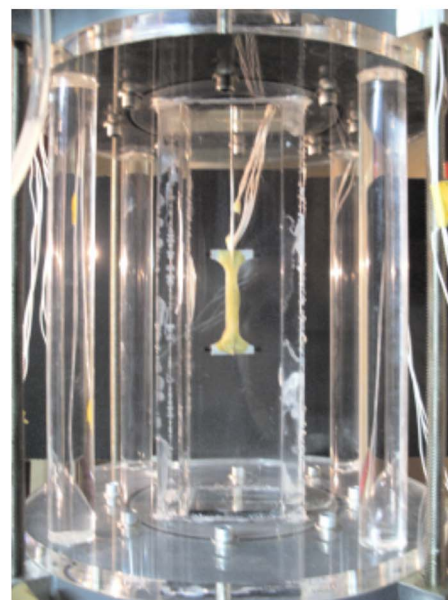
II. EXPERIMENTAL SETUP AND MEASUREMENTS

We used two different cells, both using water as the fluid. The general setup is as presented in Fig. 1. The vertical channel, in which our measurements are made, connects two chambers, a cold one at its top end and a hot one at its bottom end. Hot plumes are formed on the hot plate. They mix in the hot chamber before to feed a rising, turbulent, irregular flow in the channel. Symmetrically, cold plumes are formed on the cold plate, mix in the cold chamber, and feed a sinking flow in the channel. As will be explained below, the walls (excluding the plates), both of the chambers and of the channel, are insulating: no heat flux is entering this way.

The first cell, already described in Ref. 12, is mainly constituted of a traditional rectangular Rayleigh–Bénard (RB) cell of height 40 cm and section of 40×10 cm^2. Thanks to a honeycomb structure [made in polymethyl methacrylate[14] (PMMA)], Fig. 2(a), we avoid convection to appear in about 50% of the RB cell. The other 50%, the convection zone, has in its central part a channel with a 10×10 cm^2 cross section area ($d=10$ cm) and a height of 20 cm. This channel is our zone of interest. The walls of the RB cell are 25 mm thick PMMA.

The second cell, Fig. 2(b), has been specially designed for this experiment. It consists of two axisymmetric chambers, of conical shape, connected through a square channel, 20 cm in length, of 5×5 cm^2 inner area. The walls of the channel are made of PMMA, 10 mm thick.

For both cells, the upper plate is temperature regulated by a regulated water bath. The bottom plate is heated by the Joule effect in five resistors, regularly spaced, for the first cell, and in a heating wire, forming an Archimede spiral, for the second one. The total power input could go from 3 to 300 W to cover our range of Rayleigh numbers.

For thermal measurements, both cells are thermally insulated. The thermal insulation allows us to limit and control the heat losses in order to precisely measure the heat flux

through the cell. Heat losses can occur either via a spurious contact with the hot plate, where the Joule heating power is supplied, or through the vertical walls (or the honeycomb structure in the first cell case). Indeed, the effective heat conductivity of the channel is several thousand times that of water or plastics forming the walls. Heat would have to cross six plastic walls for flowing through the honeycomb structure. Looking at shadowgraphs of the first cell, we could verify that no activity, characteristic of convection, occurs in the honeycomb structure.

The second cell is hanged by the cold plate, whose temperature is fixed by a regulating water bath. Then, nothing except air is in contact with the hot plate. We could not hang the first cell the same way. Its hot plate fits into plastic supports. The first cell is further surrounded by a copper screen. This screen is temperature regulated at the average temperature between top and bottom plates, which is maintained constant on a whole set of measurements. In addition, both cells are wrapped in isolating sheets to limit air convection.

As a final thermal characterization of both cells, we measured the total temperature difference ΔT between the hot and cold plates, versus the supplied power. It is worth noting that this total temperature difference is the same as for a Rayleigh–Bénard cell having the same plates, and the same distance between them (within 10%). The huge constraints imposed here to the bulk flow have little influence on the global Nusselt number. This confirms previous studies[15] showing the poor influence of the bulk flow on the Nusselt number in the Rayleigh–Bénard geometry.

For vertical temperature gradient measurements, we use a bridge made of four resistive thermometers from the same batch[16] located at the corners of a rectangle 5 cm (2.5 cm) wide and of height $h=10$ cm (5 cm) for the first (second) cell. To maintain this geometry without being too intrusive, we use an "I" structure as shown on Fig. 2(b). The resistors are connected as a Wheatstone bridge, in such a way that the two upper (lower) ones are in opposite situation (no common point). As the resistors have very close temperature dependencies, the output of the bridge is poorly sensitive to the average temperature, but highly sensitive to a temperature difference between top and bottom branches of the bridge. The input to the bridge is 30 Hz, 0.1 V voltage from an Agilent 33220A generator. The output is measured by a differential lock-in amplifier Stanford Research SR830 DSP. The sensitivity of the bridge to temperature differences is typically 2 mV/K, and the order of magnitude of the output for zero temperature difference (the offset of the bridge) is 10^{-4} V. Heat losses have been estimated *in situ*, looking at the root mean squared amplitude of fluctuations of the bridge output. We extrapolate this rms amplitude to a zero value to establish the corresponding supplied power. Indeed, if the supplied power is less than heat losses, the fluid stratifies which suppresses the turbulent temperature fluctuations. Such an extrapolation also gave the exact output of the bridge for zero temperature gradient in the channel.

For temperature correlations, we used smaller resistive thermometers.[17] Both thermometers are positioned on the same vertical line, each at the bottom end of a "L" structure, the vertical bars being made of two tubes, one sliding inside

the other [Fig. 2(a)]. Both resistances r_1 and r_2 are measured through a two-wire Agilent 34970A multiplexer. Measurements have been taken by blocks of $2 \times 20\,000$. A complete measurement for a given distance between thermometers lasted two days, for nearly 100 blocks. While converting the r_i values in temperature is *a priori* possible through the calibration we made, the small amplitude of temperature fluctuations makes it useless for correlation studies. We directly consider the correlation of resistance fluctuations (see Sec. III).

Velocity fields are measured through a commercial PIV system.[18] The flow is seeded with hollow glass spheres, 10 μm in diameter.[19] Before every set of measurements, we make work the experiment some hours. Spheres with the wrong average density have time to settle at the top or the bottom of the cell. A vertical laser sheet, 2 mm wide, is obtained from a 1 W continuous laser.[20] For the first cell, a slot in one of the honeycomb structures allows the free propagation of the sheet.

We use a 30 Hz camera,[21] 1200×1600 pixels, 12 bit gray resolution. The buffer is able to store 20 frames. We thus register by blocks of 20 frames, 50 ms between frames, whose comparison gives 19 two dimensional, two components velocity fields, with 3 mm resolution. We systematically choose to register 80 such blocks, but with different spacing between blocks. The total registration time goes from 2 to 10 h.

III. CROSS-CORRELATION MEASUREMENTS

Our goal, in this study of the spatial and temporal thermal correlations is twofold. First we want to check if the correlation length ℓ is smaller than the size of the bridge, so that bridge output fluctuations can be interpreted as temperature fluctuations, a fundamental hypothesis of Ref. 12. We want also to check our second hypothesis, namely, that a [Eqs. (4) and (5)] is constant and verify its value.

We thus performed, in the first cell, the correlation measurements for two different values of the Rayleigh number, both at the same Prandtl number Pr=5.2, corresponding to an average temperature of the cell of 30 °C:

- For the high power one, the power input in the bottom plate is 235 W. Nu=1.37×10^4 and L_o=11.4 cm.
- For the low power one, the power input in the bottom plate is 23 W. Nu=4.0×10^3 and L_o=9.2 cm.

Defining $\delta r_i(t) = r_i(t) - \langle r_i \rangle$, for each distance δz between the thermometers, and each time lag τ, we calculate the correlation by averaging $\delta r_1(t+\tau)\delta r_2(t)$ first within each block, then between the blocks. We then normalize this average by the product of the rms fluctuations $\sigma_i = \sqrt{\langle \delta r_i^2 \rangle}$,

$$C(\delta z, \tau) = \frac{\langle \delta r_1(t+\tau)\delta r_2(t) \rangle}{\sigma_1 \sigma_2}. \tag{7}$$

Figure 3 presents the correlation function $C(\delta z, \tau)$ for various δz ranging from 4 mm to 10 cm, in the high power case. These functions can be seen as the sum of two components, of different amplitudes, but symmetrically shifted
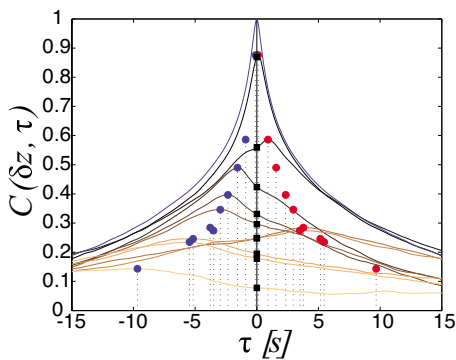
FIG. 3. (Color online) The correlation function $C(\delta z, \tau)$ for various δz in the high power case (235 W). The dots correspond to the position of the highest peak and its symmetric compared to $\tau=0$. The squares mark the value of $C(\delta z, 0)$ for the different δz, from the darker to the lighter: 4 mm, 10 mm, 20 mm, 30 mm, 40 mm, 50 mm (twice), 60 mm, 70 mm, and 100 mm. The blue (top) curve corresponds to the autocorrelation of one sensor (i.e., $\delta z=0$).

from the origin. To stress this point, we systematically signal the position of the most visible "peak," and its symmetric. Several remarks must be made.

- Each curve presents two peaks. These peaks indicate a delay between the two signals, the temperature perturbations traveling from one thermometer to the other.
- The presence of two peaks, approximately at symmetric times $\pm\tau_p$, indicates that the flow undergoes reversals. They will be discussed in Sec. V.
- From the smallest distance curves, a correlation time can be extracted. It is in very good agreement with τ_o obtained from the spectrum (Sec. IV, Fig. 5) of the bridge output fluctuations.[12]

We now turn to the correlation length ℓ. Strictly speaking, its definition assumes an exponential decay for $C(\delta z, 0)$ versus δz [$C(\delta z, 0) = \exp - (\delta z/\ell)$]. Figure 4 shows these decays for both cases, the high and the low power. Both decays
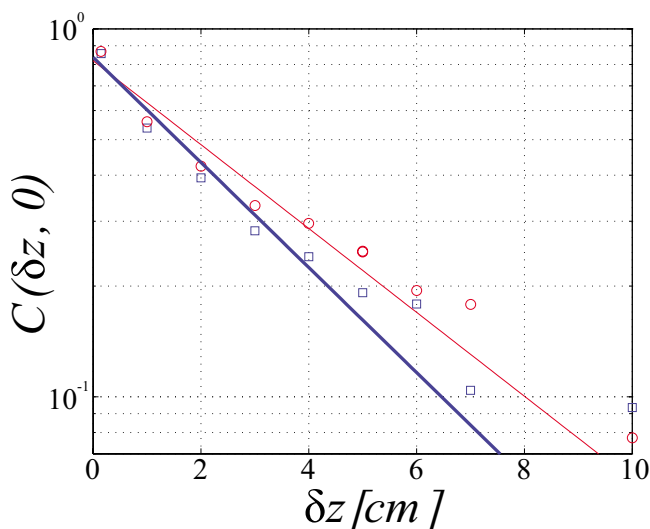

FIG. 4. (Color online) The correlation function $C(\delta z, 0)$ vs δz. The lines are fits with an exponential decay.

seem smoother than exponential, while an exponential approximation seems to be reasonable.

The best fit gives $\ell=3.8$ cm for the high power case ($L_o=11.4$ cm), and $\ell=3$ cm for the low power case ($L_o=9.2$ cm). Thus, in any case, ℓ is smaller than the height of the bridge. This confirms our first hypothesis, that the rms fluctuations of the bridge are temperature rms fluctuations and not gradient ones. Obviously, a full confirmation needs a more complete study, but the evolution of ℓ seems proportional to that of L_o.

To verify our second hypothesis, that is a is constant in Eqs. (4) and (5), we have to come back on the velocity. From the time τ_p of occurrence of the peaks, we can obtain a velocity $V_p = \delta z/\tau_p$. This velocity is independent of δz within $\pm5\%$. For the high power $V_p=1.3$ cm s^{-1}, while for the low power $V_p=0.6$ cm s^{-1}. These values are much larger than $L_o/2\tau_o$ which was the estimation of the velocity in Ref. 12. As we shall see in Sec. V, V_p is however close to the rms velocity measured using PIV in the present work. We thus must admit an error in Ref. 12, probably due to a bad calibration of distances in our first PIV measurement. We note that taking $a=1$, then $V_\theta=L/\tau_o=L_o/\tau_o$ is very close to V_p and to the rms velocity. Indeed, taking $a=1$ gives for the high power $V_\theta=1.23$ cm s^{-1}, and for the low power $V_\theta=0.62$ cm s^{-1}.

From now on, we shall thus take $a=1$, and we define

$$L = L_o = \frac{\theta}{\beta}. \tag{8}$$

We can remark here that, contrary to our intuition, ℓ/τ_o is much smaller than the rms velocity, while V_p is close to it. This suggest a peculiar organization for the coherent structures carrying the heat. Their traveling velocity as a whole is much smaller than the velocities occurring within the structure. This would be the case for a vortex, for instance, which generate velocities much larger than its own core velocity. However, the informations we have on this organization are not sufficient to go further.

To resume the results of this section, the vertical temperature correlation length ℓ is smaller than the height h of our bridge. We thus confirm that the rms output of the bridge θ must be interpreted as a temperature fluctuation amplitude, and not a gradient fluctuation amplitude. $L=\theta/\beta$ is then the intrinsic characteristic length we use in the definition of Ra and Re. It is much larger than the correlation length ℓ, suggesting a subtle organization of the flow.

IV. NUSSELT AND REYNOLDS NUMBERS

We shall systematically use the length L defined in Eq. (8) for the determination of Ra and Re, Eqs. (3) and (6). Then, it is worth discussing the real meaning of θ. The output of the Wheatstone bridge, through the sensitivity factor of 2 mV/K, measures

$$\tfrac{1}{2}[(T_3 + T_4) - (T_1 + T_2)] = T_{34} - T_{12}, \tag{9}$$

where 1 and 2 refer to the resistances at the top of the I structure [see Fig. 2(b)], 3 and 4 to those at the bottom. We just saw in the previous section that Eqs. (1) and (2) are
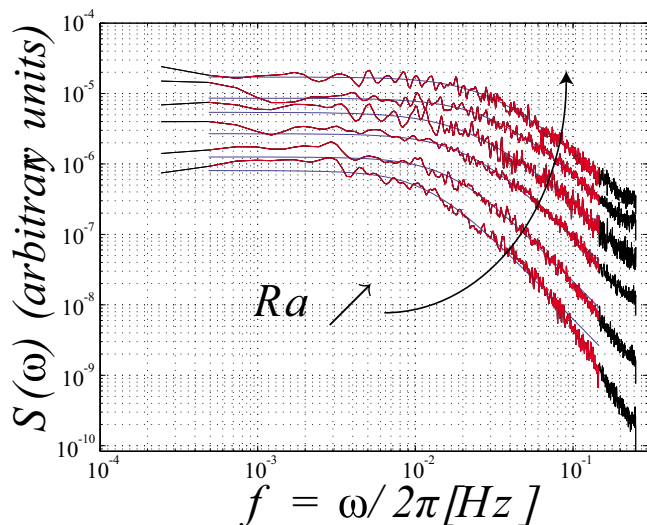
FIG. 5. (Color online) The spectra of the bridge output, for various Ra values (second cell, Pr=6). The lines correspond to the fit used for extracting τ_o. The range for the fit is signaled in red (gray) on the spectrum.
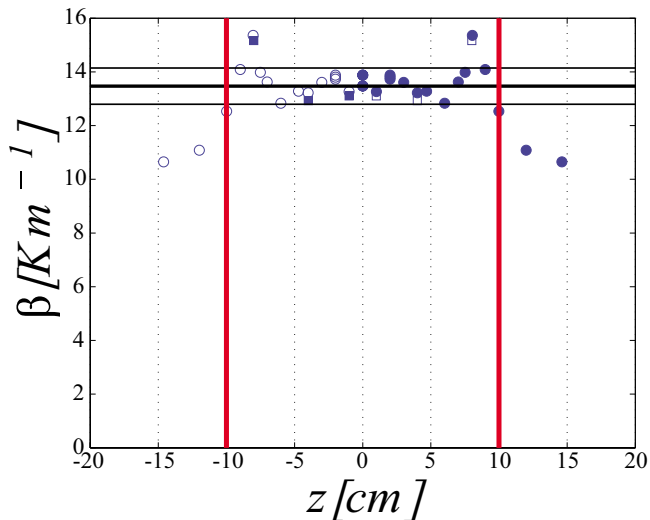

FIG. 6. (Color online) Temperature gradient vs the height in the cell, for the second cell. Only full symbols correspond to real measurements. Open symbols are simply symmetric to the full ones compared to the middle of the cell. The two vertical bars signal the ends of the channel. The thick horizontal line stands for the average of $\beta(z)$ in the center of the channel. The lower and upper horizontal lines correspond to $\pm 5\%$ of this mean value.

decorrelated from Eqs. (3) and (4), their vertical distance h (10 cm for the first cell, 5 cm for the second one) being larger than the correlation length.

At this point, it is useful to briefly discuss the structure of the flow and the temperature field, which will be detailed in Sec. V. A large scale flow is present in the channel, ascending on one side and descending on the other, with occasional reversals, already mentioned. This flow creates a temperature difference between both sides of the I structure, at the same level, this difference, of absolute value 2Δ, changing its sign at each reversal. Indeed, the rising flow, coming from the hot chamber, is slightly warmer $(+\Delta)$ than the sinking flow, coming from the cold chamber $(-\Delta)$. The time between these reversals can be long, 10 min or more. As a result, T_1 and T_2 are correlated, the fluctuations of $T_{12}=(T_1+T_2)/2$ being poorly sensitive to the reversals dynamics. The mean squared deviation of the bridge output then gives

$$\theta^2 = \langle \delta T_{34}^2 \rangle + \langle \delta T_{12}^2 \rangle = 2\langle \delta T_{12}^2 \rangle. \tag{10}$$

θ is thus different from the local rms temperature fluctuations, due to the reversals. The frequency spectrum of the bridge output is also different in shape from the local temperature one, particularly in its low frequency part, sensitive to the reversals dynamics.

We recall that this spectrum gives us the time τ_o, from which we obtain the Reynolds number through Eq. (6). Figure 5 shows a series of such spectra, corresponding to various Rayleigh numbers.

In order to improve the precision on τ_o we used a fit of these spectra $S(\omega)$. Indeed, considering $\omega S(\omega)$ gives a maximum in the neighborhood of $\omega_o=1/\tau_o$. We thus fit $\omega S(\omega)$ with the function

$$S_o \frac{\omega\tau_\gamma}{1+(\omega\tau_\gamma)^\gamma}, \tag{11}$$

where S_o, τ_γ and γ are adjustable parameters. In fact, the optimum γ has very little variation, close to 1.8 for the first

cell, and 2 for the second one. For each cell, we thus used the same γ for all spectra. We define the characteristic time τ_o as

$$\tau_o = (\gamma-1)^{1/\gamma}\tau_\gamma. \tag{12}$$

In this way, two fits having their maximum at the same frequency give the same value for τ_o, whatever γ is.

In Ref. 12, we checked the vertical homogeneity of the gradient β in the channel for the first cell. We made the same test in the second cell, measuring the gradient at various heights. Figure 6 gives the results, for a driving power of 80 W, and a mean temperature of 25 °C.

Positions between -10 and 10 cm correspond to the center of the bridge being in the channel. Between -20 and -10 cm it is in the hot chamber, and in the cold one between 10 and 20 cm. Compared to the first cell,[12] the conical shape of the chambers seems to result in a significant vertical gradient in these chambers. Correlatively, the channel end effect is strongly reduced, and the gradient can be considered as constant on a large range around the middle of the cell. Note also the large value of the gradient here $(\beta=13.5 \text{ K m}^{-1})$. For the same power (80 W) and the same temperature (25 °C), the gradient is $\beta=1.9 \text{ K m}^{-1}$ in the first cell. This measurement confirms that in the central part of the channel, the temperature gradient β is constant within less than $\pm 5\%$.

We now come to the presentation of our results, for Nu and Re Pr versus Ra Pr. The various symbols on Fig. 7 correspond to different mean temperatures, and thus different Prandtl numbers Pr: 20 °C, Pr=6.6; 30 °C, Pr=5.3; 40 °C, Pr=4.1. The lower Ra Pr (diamonds) correspond to the second cell and a mean temperature of 25 °C (Pr=6). The error bars on Nu are based on an estimated uncertainty of 0.5 W on the heat leaks, and 2×10^{-3} °C uncertainty on the temperature difference measured by the bridge. The latter uncertainty also gives that of β which, together with 2% on θ yield the error bars on L and Ra (see Fig. 8).
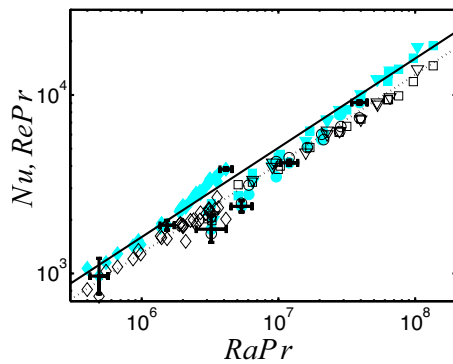
FIG. 7. (Color online) Evolution of Nu (full symbols) and Re Pr (open symbols) vs Ra Pr. First cell: ($\bigcirc$) Pr=6.6; ($\triangledown$) Pr=5.3; ($\blacksquare$) Pr=4.1. Second cell: ($\diamond$) Pr=6. Full line, proposed average law for Nu results: Nu $=1.6\sqrt{\text{Ra Pr}}$. Dotted line, proposed average law for Re Pr results: Re Pr $=1.3\sqrt{\text{Ra Pr}}$

We note the good agreement for the Re results between the two cells, and for both cells, with a law

$$\text{Re Pr} \simeq 1.3\sqrt{\text{Ra Pr}}. \qquad (13)$$

We remark that this agreement does not depend on the chosen value for L, due to our definition of Re, Eq. (6). The above law indicates that the velocity does not depend on the diffusivity κ, but depends on the viscosity ν through the dependence of L versus Re (see below, Fig. 8).

As for the heat transport, despite the large differences noted above for temperature gradients between the two cells, they agree when normalized as Nu. A common law could be

$$\text{Nu} \simeq 1.6\sqrt{\text{Ra Pr}}. \qquad (14)$$

Note, however, that the tendency within each cell, is to a steeper logarithmic slope, but the difference with 1/2 is close to the error bar. Here, the agreement between cells strongly depends on the choice of L. We used the same rule, Eq. (8), for its determination in the second cell. It gives a roughly constant value, close to d. Figure 8 resumes the variations of L/d for both cells versus Re, showing the agreement between them. It also confirms the existence of the threshold Re$* \simeq 600$. For Re$<$Re$*$, L/d is constant, For Re$>$Re$*$, L/d increases with Re, approximately linear in ln Re.
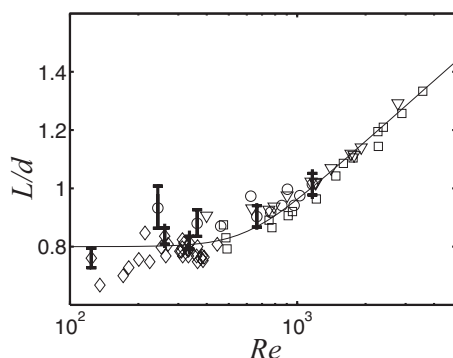

FIG. 8. Dependence of L/d vs Re for both cells. Same symbols as in Fig. 7. The line correspond to a fit of our data with the formula: $(L/d) = 0.075 \ln[1 + (\text{Re}/\text{Re}*)^4] + 0.8$, with Re$* = 600$.

Can we compare with the results of the numerical simulation of 10? The difficulty is in the choice of the characteristic length. In Ref. 10, periodic boundary conditions are used, and the characteristic length is the period of the system. In our case, we shall see in Sec. VI that a half sine period can fit the vertical velocity x-profile, the period being 18 cm, i.e., approximately $2d$. For a valuable comparison, their Ra values should be divided by $2^4 = 16$ and their Re values by 2. Then, the laws they propose, Nu $\simeq 0.7\sqrt{\text{Ra}}$ and Re $\simeq 1.1\sqrt{\text{Ra}}$ (Pr=1) must be read

$$\text{Nu} \simeq 2.8\sqrt{\text{Ra}}; \quad \text{Re} \simeq 2.2\sqrt{\text{Ra}}. \qquad (15)$$

Considering the uncertainty on this conversion factor, the agreement is not bad. In particular, the ratio Re/Nu agrees well. There remains a difference of almost a factor 2 on both Nu and Re. Is it due to their absence of confinement in x which favors velocity fluctuations, or to the periodicity in z which prevents the free formation of plumes? The answer matters if we have to correctly model free convection in stars or atmospheres, but it will need further studies.

We can also compare with the results of Ref. 11. They look at the transient free convection in a vertical tube connecting two chambers with different salt concentrations. Thus, they have a flux of salt instead of a flux of heat, and the salt diffusion coefficient (the Schmidt number Sc) takes the place of κ (Pr). They obtain

$$\text{Nu} \simeq 0.88\sqrt{\text{Ra Sc}}; \quad \text{Re Sc} \simeq \sqrt{\text{Ra Sc}}, \qquad (16)$$

The agreement with our results is good if we consider that they take d as the characteristic length scale, which is slightly larger than our L (their Reynolds number is small, lower than the threshold Re$*$). Moreover, they do not measure directly the density gradient in the tube, but estimate it from the difference in salt concentration between the chambers.

To resume the results of this section, the Nu and Re dependences versus Ra and Pr are coherent with a purely inertial behavior, if $L = \theta/\beta$ is the characteristic length entering the definition of Ra and Re. It means that the heat flux and the fluid velocity do not depend on the heat molecular diffusivity, and that their dependence on the kinematic viscosity is entirely contained in the Re dependence of L. This dependence changes at some threshold Re$* \simeq 600$. For Re $<$ Re$*$, L is constant and close to d. Previous equivalent studies[10,11] fit into this regime and we reasonably agree with them. For Re $>$ Re$*$, L grows, approximately linear in ln Re. Can we extrapolate this dependence up to the largest Re, or do some saturation occurs? We presently do not know.

V. DESCRIPTION OF THE VELOCITY FIELD

In this section, we describe the velocity field as obtained through our PIV system.[18] As visualizing the cell prevents us to use the thermal screen, the average fluid temperature is chosen to be that of the room (30 °C), and only the bottom plate is thermally coated. Most of the measurements have been made with the first cell. The second one has been used for checking some of the conclusions.
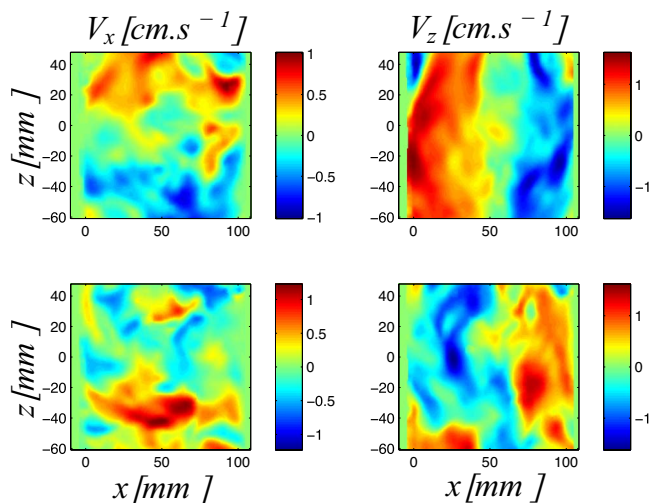
FIG. 9. (Color online) Two typical instantaneous maps of the two velocity components algebraic values. Note that the color code is not the same for v_x and v_z. Top: $\epsilon = +1$. Bottom: $\epsilon = -1$ (see text).

As seen in Ref. 12, the channel ends effects influence the flow a few centimeters from these ends. It is why we limit our study in the first cell to the range $-5 \text{ cm} < z < 5 \text{ cm}$. As we shall see later, even in this restricted range, ends have a visible, but negligible, effect.

Two different input powers have been explored, 180 W (Ra$=1.51\times10^7$) and 93 W (Ra$=7.9\times10^6$). The discussion below will mainly concern the lowest. Figure 9 shows typical instantaneous maps of the two components, v_x and v_z.

In most of the pictures, for this first cell, the flow is globally ascending in the left hand part, and descending in the right one (as in Fig. 9, top), or the opposite (Fig. 9, bottom). These flows, we call Φ-flows. Some of the pictures show a flow globally ascending in both parts (remember that we record only a sheet of the flow), or descending. We call this kind of flow Ξ-flows. Φ-flows have a typical mixing layer structure. In order to discuss them, we have first to extract the average profile of the velocity field.

With this in mind, we first define ϵ_l, which is 1 if the average of the vertical velocity in the left part is positive, and $\epsilon_l = -1$ if it is negative. We also define ϵ_r which is -1 if the average of the vertical velocity in the right part is positive, and $\epsilon_r = 1$ if this latter average is negative. For Φ-flows, $\epsilon_l = \epsilon_r$. Reciprocally, for Ξ-flows, $\epsilon_l = -\epsilon_r$. We then define

$$\epsilon = (1/2)(\epsilon_l + \epsilon_r), \tag{17}$$

which is zero for Ξ-flows, and ±1 for Φ-flows.

Figure 10 shows $\epsilon(t)$ for a 2 h period record at 93 W. As explained in Sec. II, these records consist of 80 blocks of 19 instantaneous velocity maps, the duration of a block being 1 s. The interval between blocks is thus 89 s. Clearly, this record shows no characteristic time. The dynamics of these reversals will be studied in another paper.

Figure 11 shows the average fields $\langle \epsilon v_x \rangle$ and $\langle \epsilon v_z \rangle$ where $\langle \rangle$ stands for time average divided by the time average of ϵ^2, to take into account only the Φ flows. $\langle \epsilon v_z \rangle$ presents a reasonable invariance versus z, as expected for the central part of the channel. In contrast $\langle \epsilon v_x \rangle$ shows unexpected nonzero
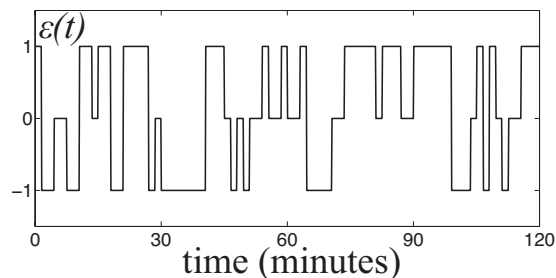
average at top and bottom parts, as if a roll was superimposed to the expected parallel flow. Note however that the amplitude of this roll is much weaker than the parallel component. Moreover, a comparison with the velocity field in the second cell shows that these finite average horizontal velocity spots follow the channel ends when the relative distance between them increases. We can thus consider them as a trace of end effects.

Due to the observed translational invariance, it is reasonable to define the z-average

$$U_z(x) = \overline{\langle \epsilon v_z \rangle}^z \tag{18}$$

as the profile of the vertical velocity. Here $\overline{\langle . \rangle}^z$ stands for a time average, itself averaged along z.

As for the x component, let us define

$$U_x(x) = \sqrt{\overline{(\langle \epsilon v_x \rangle)^2}^z}, \tag{19}$$

which will be useful when looking at fluctuations, in Sec. VI. Moreover, comparing them on the same graph, Fig. 12 allows to estimate the relative importance of this artifact.
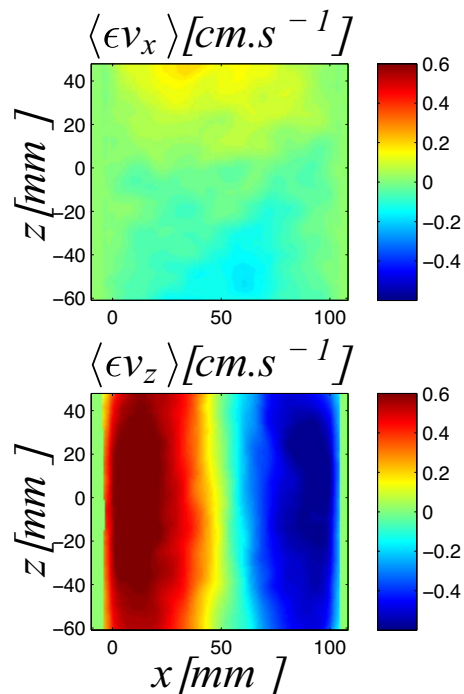

FIG. 10. Schematic dynamics of the reversals.
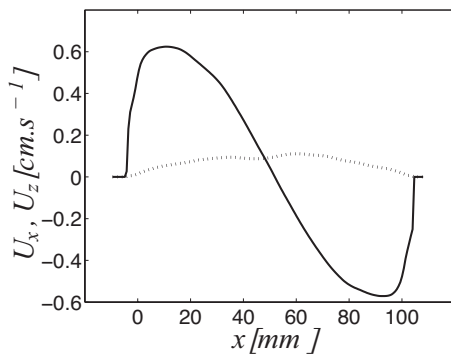

FIG. 11. (Color online) Time averages of ϵv_x and ϵv_z.

FIG. 12. U_z (full line) and U_x (dotted line) profiles. See the text for the definition of these z and time averages.

FIG. 13. (Color online) The Reynolds stresses τ_{xx} ($\bigcirc$), τ_{zz} ($\bigtriangledown$), and τ_{xz} ($\triangle$), vs x, for the lowest power (93 W). The full symbols correspond to the range of the fit ($x_-=7$ mm, $x_+=94$ mm). The lines show the proposed fit.

To resume the results of this section, apart from erratic reversals, the mean flow organizes in two columns, of rising hot fluid and sinking cold fluid. The nonzero horizontal velocity averages clearly identify as end effects.

VI. VELOCITY AND TEMPERATURE FIELDS: LOCAL BUDGETS

The study of the velocity field we have made allows more than determining an average profile. It allows to look at the Reynolds stresses induced by the fluctuations, which, in turn, give indirect information about the horizontal temperature profile:

$$\Theta(x) = \overline{\langle \epsilon T \rangle^z}. \tag{20}$$

Indeed, the momentum budget along the vertical direction is, within the Boussinesq approximation,

$$\partial_t v_z + \partial_j \left(v_z v_j + \frac{p}{\rho}\delta_{z,j} - \nu \partial_j v_z \right) = g\alpha T, \tag{21}$$

where repeated index j means summation on $j = x, y, z$, and $\delta_{z,j}$ is the Kronecker symbol. To be specific, p is the effective pressure, including the potential term $\rho g z$. ρ is the fluid density under this pressure and a temperature equal to the time averaged and horizontally averaged one at $z=0$. Multiplying Eq. (21) by ϵ, and averaging over t and z gives

$$\partial_x (\overline{\langle \epsilon v_x v_z \rangle^z} - \nu \partial_x U_z) = g\alpha\Theta. \tag{22}$$

Indeed, to obtain Eq. (22) we also average over y, the third dimension. In the experimental PIV study, we had only access to a sheet, and we assumed the statistical invariance along y. From now on, we shall consider that the subscript $*$ systematically implies an average on y.

Equation (22) alone shows the importance of $\tau_{xz} = \overline{\langle \epsilon v_x v_z \rangle^z}$ which represents the momentum flux along x when the viscosity can be neglected. Figure 13 shows the x variations of τ_{xz}, together with the two other significant Reynolds stresses: $\tau_{zz} = \overline{\langle (\epsilon v_z - \langle \epsilon v_z \rangle)^2 \rangle^z}$ and $\tau_{xx} = \overline{\langle (\epsilon v_x - \langle \epsilon v_x \rangle)^2 \rangle^z}$. Indeed, the last two play little role as stresses, but give a good estimate of the amplitude of the fluctuations.

Several remarks can be made. First, τ_{xz} is much larger than the viscous stress $|\nu \partial_x U_z|$ (2.5×10^{-3} cm^2 s^{-2} in the center), except very close to the walls (where anyway the precision of our PIV is doubtful). It means that most of the
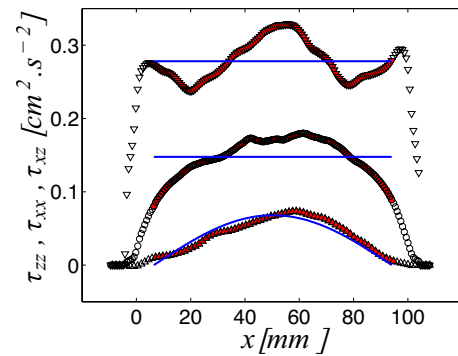
momentum created by the buoyancy forces directly exchange from one side of the channel to the other, with almost nothing going to the walls. We can practically neglect the friction on the walls.

Second, τ_{xx} and τ_{zz} are almost constant across the channel, suggesting a kind of homogeneity in the "turbulent fluid" which we study. However, $\tau_{zz} > \tau_{xx}$. This turbulent fluid is anisotropic. Finally, note that τ_{zz} is of the order of U_z^2. The vertical velocity fluctuations are large.

We can also write the enthalpy budget in the channel,

$$C_p \partial_t T + \partial_j (q_j + v_j C_p T) = 0, \tag{23}$$

where C_p is the constant pressure heat capacity per unit volume, and $\vec{q}$ is the diffusive heat flux. Writing

$$\vec{Q} = \vec{q} + C_p T \vec{v}, \tag{24}$$

the total heat flux, diffusive plus convective, we note that Q_x changes its sign at each reversal, on average, while Q_z does not. Then, multiplying Eq. (23) by ϵ, and averaging on t and z gives

$$C_p \beta U_z = \partial_x \overline{\langle \epsilon Q_x \rangle^z}, \tag{25}$$

giving indirect access to the horizontal heat flux $\overline{\langle \epsilon Q_x \rangle^z}$. To obtain this result, it is convenient to define $\vec{v}'$ and T' such that

$$\epsilon(T + \beta z) = \Theta(x) + T'$$

$$\epsilon v_x = v_x' \tag{26}$$

$$\epsilon v_z = U_z(x) + v_z'.$$

$\vec{v}'$ and T' have zero average, and their statistics and correlation are independent of z.

The relative constancy of τ_{xx} and τ_{zz} suggests, as discussed in Sec. VII, to define effective transport coefficients for this quasihomogeneous turbulent fluid. For instance, we can define a "turbulent viscosity" through the relation

$$\overline{\langle \epsilon v_x v_z \rangle^z} = -\nu^{\text{turb}} \frac{dU_z}{dx}. \tag{27}$$

Having access, both, to the temperature profiles and to the heat fluxes in the vertical and horizontal directions, effective heat conductivities can be defined as follows:

$$\overline{Q_z}^x = Q = \frac{C_p}{d}\int_0^d U_z(x)\Theta(x)dx + k_z^{\text{turb}}\beta, \qquad (28)$$

$$\overline{\langle\epsilon Q_x\rangle}^z = -k_x^{\text{turb}}\frac{d\Theta}{dx}. \qquad (29)$$

However, with the small statistics we have, and the corresponding noise on averaged quantities we cannot directly use Eqs. (27)–(29). It is why we smooth the obtained profiles through a simplified model.

We model the major central part of the flow, letting aside two regions $x < x_-$ and $x_+ < x$ as "boundary layers" close to the vertical walls. Considering that the momentum flux toward the walls is very small, a stress-free boundary flow well fits the profile of the vertical velocity,

$$U_z(x) = U\cos\left(\pi\frac{x-x_-}{x_+ - x_-}\right). \qquad (30)$$

We can then determine ν^{turb}, using Eq. (27), and approximating $\tau_{xz}(x)$ with a sine function,

$$\overline{\langle\epsilon v_x v_z\rangle}^z = \tau_{xz,o}\sin\left(\pi\frac{x-x_-}{x_+ - x_-}\right), \qquad (31)$$

with

$$\tau_{xz,o} = \nu^{\text{turb}}\frac{\pi U}{(x_+ - x_-)}. \qquad (32)$$

Having ν^{turb}, we can return to Eq. (22), and determine

$$\Theta(x) = (\nu^{\text{turb}} + \nu)\frac{\pi^2 U}{g\alpha(x_+ - x_-)^2}\cos\left(\pi\frac{x-x_-}{x_+ - x_-}\right)$$
$$= \Theta_o\cos\left(\pi\frac{x-x_-}{x_+ - x_-}\right). \qquad (33)$$

Finally, using Eqs. (25) and (29), we can determine k_x^{turb},

$$k_x^{\text{turb}} = C_p\beta\frac{(x_+ - x_-)^4}{\pi^4}\frac{g\alpha}{\nu^{\text{turb}} + \nu}. \qquad (34)$$

The relative values of these effective transport coefficients, and their physical interpretation, will be discussed in Sec. VII. Let us here briefly discuss the precision we can expect on them. We shall first consider the bounds of the fits, x_+ and x_-, as given, and discuss later the influence of their choice.

The averages are obtained from 80 blocks of 20 frames. The simple fact that the sign of ϵ is clear on each block shows that the error bar on each quadratic quantity obtained from a single block is smaller than its mean value. We estimate this error bar to be half the mean value. Averaging on 80 blocks thus yield to 6% on each quadratic quantity, and 3% on their square root. The precision on β is estimated at 2%. All these estimates obviously hold for reasonably high input power, where heat leaks are negligible.

The precision on ν^{turb} is limited by the precision on U and that on τ_{xz}. Following the above discussion it should be 7%. The precision on Θ_o is simply limited by the precision on τ_{xz}, that is 6%. The precision on k_x^{turb} depends on β and ν^{turb}. We thus estimate it as 7%.

As ν^{turb} is much larger than ν, and considering its precision, ν will always be negligible compared to ν^{turb}. Another quantity of interest will be the turbulent Prandtl number,

$$\text{Pr}^{\text{turb}} = \frac{C_p\nu^{\text{turb}}}{k_x^{\text{turb}}}. \qquad (35)$$

The above discussion yield to 10% precision on Pr^{turb}.

Let us now discuss on the influence of x_+ and x_-. Indeed, we remarked that their choice have very little influence on the calculated value of ν^{turb}. This was to be expected, as ν^{turb} is obtained from the comparison of two really measured quantities, $U_z(x)$ and $\tau_{xz}(x) = \overline{\langle\epsilon v_x v_z\rangle}^z$. The values proposed for ν^{turb} should thus be reliable, within their estimated uncertainty. The consequence, however, is that k_x^{turb} behaves as $(x_+ - x_-)^4$ [see Eq. (34)].

We thus proceed as follows. We define symmetrized versions of the data, namely,

$$U_{\text{sym}}(x) = (U_z(x) - U_z(d-x))/2 \qquad (36)$$

and

$$\tau_{\text{sym}}(x) = (\tau_{xz}(x) + \tau_{xz}(d-x))/2, \qquad (37)$$

and we call dU and $d\tau$ the root mean squared differences between these symmetrized data and the sine approximations. We then search for the minimum of $(d\tau/\tau_{xz,o})^2 + 4(dU/U)^2$ versus $(x_+ - x_-)$. This minimum, mainly dominated by $d\tau$, is sufficiently peaked as to consider $(x_+ - x_-)$ as determined within less than 2%.

In this section, we showed that the mean flow is coherent with the most simple model, implying constant effective diffusivities and stress-free boundary conditions. Measuring the Reynolds stresses give us access to the horizontal temperature profile and to the horizontal corresponding heat flux. Concrete values, and an interpretation of the measured turbulent diffusivities, are given in Sec. VII.

VII. MIXING LENGTHS AND PLUMES

In this section, we examine the pertinence of effective transport coefficients to describe our turbulent fluid. Having in mind a comparison with the kinetic theory of gases, a transport coefficient like ν^{turb} can be seen as the product of the characteristic velocity of fluid particles (the momentum carriers) with a characteristic length, the Prandtl's "mixing length." As the corresponding transport is along the x axis, we can take $\sqrt{\tau_{xx}}$ as the characteristic velocity, and write

$$\nu^{\text{turb}} = L_\nu\sqrt{\tau_{xx}}. \qquad (38)$$

Such a description makes sense only if L_ν is smaller than the characteristic length of the mean flow, of order d. In the same spirit, we can write

$$k_x^{\text{turb}} = C_p L_{kx}\sqrt{\tau_{xx}} \qquad (39)$$

and

TABLE I. Summary of the various quantities directly measured or derived from the measurements for two experiments at the average temperature of 30 °C, in the first cell. The last column allows to distinguish between the approximately constant quantities and the varying ones.

Quantity X	93 W	180 W	$\Delta X/X_m$ (%)
$\mathrm{Pr}=\nu/\kappa$	5.22	5.12	-2
β (K m^{-1})	1.82	2.39	27
L (cm)	10.1	11.1	9
V_θ (m s^{-1})	8.9×10^{-3}	1.18×10^{-2}	9
Nu	8300	12 200	38
Ra	5.4×10^{6}	1.03×10^{7}	63
Re	1170	1730	39
x_- (mm)	7.1	5.4	-27
x_+ (mm)	93.4	94.9	2
U (m s^{-1})	6.2×10^{-3}	7.6×10^{-3}	20
τ_{zz} (m^2 s^{-2})	2.8×10^{-5}	4×10^{-5}	35
τ_{xx} (m^2 s^{-2})	1.5×10^{-5}	2.1×10^{-5}	33
$\tau_{xz,o}$ (m^2 s^{-2})	0.68×10^{-5}	1.0×10^{-5}	39
Θ_o (K)	0.079	0.112	35
ν^{turb} (m^2 s^{-1})	3.00×10^{-5}	3.77×10^{-5}	23
k_x^{turb}/C_p (m^2 s^{-1})	1.1×10^{-4}	1.3×10^{-4}	18
$\mathrm{Pr}^{\mathrm{turb}}$	0.28	0.29	4
k_z^{turb}/C_p (m^2 s^{-1})	0.93×10^{-3}	1.38×10^{-3}	39
L_ν (cm)	0.78	0.83	6
L_{kx} (cm)	2.8	2.9	2
L_Q (cm)	17.6	21.8	21

$$k_z^{\mathrm{turb}} = C_p L_Q \sqrt{\overline{\tau_{zz}}}. \tag{40}$$

Table I compares two experiments at the average temperature of 30 °C, with the total applied power of 93 and 180 W, in the first cell. $\Delta X/X_m$ refers to the difference between the considered quantity values in both cases, divided by their mean value. $V_\theta = L/\tau_o$.

Let us comment first on the values of x_+ and x_-. They are close to the walls, the closer when the Reynolds number is higher. The relative size of the "boundary layer" is smaller when Re is larger as one could have expected. Thus the process we followed to determine x_+ and x_- gives reasonable values.

Looking at the last column, we see that some quantities exhibit changes larger than the error bar, other not. Specifically, we note that $\mathrm{Pr}^{\mathrm{turb}}$ is the same in both cases. Qualitatively, a value close to 1 had to be expected, as the carriers of both momentum and energy are the fluid particles themselves. The value obtained, 0.28 ± 0.03 differs sufficiently from 1 to be nontrivial. For example, the Prandtl number of a monatomic gas as helium is $\mathrm{Pr}=0.7$.

The "mixing lengths" show contrasting behaviors. L_ν and L_{kx} are short, much smaller than d, and can be considered as constant. They correspond to the expected properties of such quantities. It means that their values can be used for predicting the effective transport coefficients ν^{turb} and k_x^{turb}, and that these effective coefficients can yield to meaningful predictions, concerning the average flow.

Conversely, the values of L_Q are not compatible with a

mixing length approach. If we refer again to the kinetic theory of gases, these values suggest a "Knudsen" regime, where the mean free path of the carriers is larger than the size of the experiment. It is then more convenient to focus on the behavior of "individual carriers." This is such a model that we develop below.

In a very schematic point of view, let us then consider that heat is carried by intermittent coherent flows, which we call plumes. The velocity intensity of such a plume will be called ν and the temperature intensity ϑ, in such a way that the instantaneous heat flux carried by the plume is

$$Q = C_p \nu \vartheta/2. \tag{41}$$

Now, let us call ϖ the probability to be in a plume at a given point and time in the channel. The total heat flux will be

$$Q = \varpi \mathcal{Q}, \tag{42}$$

while the amplitude of the average flow U, and of the horizontal temperature profile Θ_o will be

$$U = \varpi \nu; \quad \Theta_o = \varpi \vartheta. \tag{43}$$

We can thus estimate ϖ, through

$$\varpi = \frac{C_p U \Theta_o}{2Q}. \tag{44}$$

Both experiments presented in the above table give estimates of ϖ in the neighborhood of 14%. This ratio can also be seen as the part of the heat carried by the mean flow. In this respect, we can say that most of the heat is carried by plumes and not by the mean flow. Recent studies in Rayleigh–Bénard cells [8,9] yield to the same conclusion.

VIII. CONCLUSION

In this paper, we have extended our previous measurements to another cell, of different sizes and aspect ratios, and found good agreement between the results of both cells. We also have studied the structure of the flow, both the mean flow and the fluctuations.

The temperature fluctuations, and their correlations, confirmed the hypothesis of short correlation length we made previously. However, it also showed that the ratio between the correlation length ℓ and the correlation time τ_o is much smaller than the rms velocity. Certainly, further studies are necessary in order to confirm the impression we have that both have parallel behaviors versus Ra and Pr. In any case, this only result shows that the organization of the coherent structures carrying the heat is very peculiar and has to be elucidated.

The mean flow appeared to be rather simple, if we disregard the reversals which will be the object of another work. The flow appears to be governed by effective horizontal transport coefficients ν^{turb} and k_x^{turb}, the corresponding mixing lengths being much smaller than the size of the channel. The effective turbulent fluid appears as homogeneous on roughly the whole width of the channel. It seems to be a scholar example for such concepts.

Conversely, the vertical heat transport cannot be modeled through an effective vertical heat conductivity. The good picture is more a transport by individual plumes. Again, further studies are needed to fully characterize these plumes.

ACKNOWLEDGMENTS

[1] E. Siggia, "High Rayleigh number convection," Annu. Rev. Fluid Mech. **26**, 137 (1994).

[2] X. Chavanne, F. Chillà, B. Chabaud, B. Castaing, and B. Hébral, "Turbulent Rayleigh-Bénard convection in gaseous and liquid He," Phys. Fluids **13**, 1300 (2001).

[3] S. Grossmann and D. Lohse, "Scaling in thermal convection: A unifying view," J. Fluid Mech. **407**, 27 (2000); S. Grossmann and D. Lohse, "Fluctuations in Rayleigh-Bénard convection: The role of plumes," Phys. Fluids **16**, 4462 (2004).

[4] X. Chavanne, F. Chillà, B. Castaing, B. Hébral, B. Chabaud, and J. Chaussy, "Observation of the Ultimate Regime in Rayleigh-Bénard Convection," Phys. Rev. Lett. **79**, 3648 (1997).

[5] J. J. Niemela, L. Skrbek, K. R. Sreenivasan, and R. J. Donnelly, "Turbulent convection at very high Rayleigh numbers," Nature (London) **404**, 837 (2000).

[6] J. J. Niemela and K. R. Sreenivasan, "Confined turbulent convection," J. Fluid Mech. **481**, 355 (2003).

[7] R. H. Kraichnan, "Turbulent thermal convection at arbitrary Prandtl number," Phys. Fluids **5**, 1374 (1962).

[8] X. D. Shang, X. L. Qiu, P. Tong, and K. Q. Xia, "Measured local heat transport in turbulent Rayleigh-Bénard convection," Phys. Rev. Lett. **90**, 074501 (2003).

[9] Y. Gasteuil, W. Shew, M. Gibert, F. Chillà, B. Castaing, and J. F. Pinton, "Lagrangian temperature, velocity and local heat flux measurements in Rayleigh Bénard convection," Phys. Rev. Lett. **99**, 234302 (2007).

[10] D. Lohse and F. Toschi, "Ultimate state of thermal convection," Phys. Rev. Lett. **90**, 034502 (2003); E. Calzavarini, D. Lohse, F. Toschi, and R. Tripiccione, "Rayleigh and Prandtl number scaling in the bulk of Rayleigh-Bénard turbulence," Phys. Fluids **17**, 055107 (2005).

[11] M. R. Cholemari and J. H. Arakeri, "Experiments and a model of turbulent exchange flow in a vertical pipe," Int. J. Heat Mass Transfer **48**, 4467 (2005).

[12] M. Gibert, H. Pabiou, F. Chillà, and B. Castaing, "High Rayleigh number convection in a vertical channel," Phys. Rev. Lett. **96**, 084501 (2006).

[13] F. Perrier, P. Morat, and J. L. Le Mouel, "Dynamics of air avalanches in the access pit of an underground quarry," Phys. Rev. Lett. **89**, 134501 (2002).

[14] PMMA: PolyMethylMethAcrylate.

[15] S. Ciliberto, S. Cioni, and C. Laroche, "Large-scale flow properties of turbulent thermal convection," Phys. Rev. E **54**, R5901 (1996).

[16] Typical values are 2 kΩ at 20 °C, and 1 kΩ at 40 °C.

[17] Typical values are 30 Ω at 20 °C, with 0.5 Ω/K sensitivity, 0.4 mm in size.

[18] Davis-7, LaVision, GmbH.

[19] Sphericel 110P8, LaVision, GmbH.

[20] DPSS-Laser System, 532 nm, Melles Griot.

[21] Imager Pro, LaVision, GmbH.